Version: Correction

Word Count: 8388

Distribution of REE between amphibole and pyroxenes in the lithospheric mantle: An assessment from the lattice strain model

Chunguang Wang[1,*], Yan Liang[2], Wenliang Xu[1], Chenguang Sun[3], and Kei Shimizu[4]

1. College of Earth Sciences, Jilin University, Changchun 130061, China
2. Department of Earth, Environmental and Planetary Sciences, Brown University, Providence, RI 02192, USA
3. Department of Geological Sciences, Jackson School of Geosciences, University of Texas at Austin, Austin, TX 78712, USA
4. WiscSIMS, Department of Geoscience, University of Wisconsin–Madison, Madison, WI 53706, USA

*Corresponding author: c_wang@jlu.edu.cn

Appendix A. Parameters in the lattice strain models for REE partitioning between amphibole, pyroxenes, and silicate melts.

Appendix B. Parameters in the semi-empirical models for amphibole temperature

Appendix C. Online Supplementary Text S1–S2, Table S1–2, and Figures S1–S24.

Appendix D. Excel calculator for pyroxene-amphibole REE partition coefficients.

Abstract

Amphibole and pyroxenes are the main reservoirs of rare earth elements (REEs) in lithospheric mantle that has been affected by hydrous metasomatism. In this study, we developed semi-empirical models for REE partitioning between orthopyroxene and amphibole and between clinopyroxene and amphibole. These models were formulated on the basis of parameterized lattice strain models of mineral–melt REE partitioning for orthopyroxene, clinopyroxene, and amphibole, and they were calibrated using major element and REE data of amphibole and pyroxenes in natural mantle samples from intraplate setting. The mineral–melt REE partitioning models suggest that amphibole is not in equilibrium with coexisting pyroxenes in the mantle samples, and that the amphibole crystallized at a lower temperature than that of the pyroxenes. We estimated the apparent amphibole crystallization temperature using major element compositions of the amphibole and established temperature- and composition-dependent models that can be used to predict apparent pyroxene–amphibole REE partition coefficients for amphibole-bearing peridotite and pyroxenite from intraplate lithospheric mantle. Apparent pyroxene–amphibole REE partition coefficients predicted by the models can be used to infer REE contents of amphibole from REE contents of coexisting pyroxenes. This is especially useful when the grain size of amphibole is too small for trace element analysis.

Keywords: amphibole, clinopyroxene, orthopyroxene, peridotite, pyroxenite, REE partitioning, temperature, mineral composition

Introduction

The lithospheric mantle is composed mainly of nominally anhydrous minerals, including olivine, orthopyroxene, clinopyroxene, spinel, and garnet. Hydrous minerals such as amphibole and phlogopite, are also present in regions that have been affected by modal metasomatism. Amphibole can be formed by the interaction between peridotite and hydrous melts (e.g., Sen and Dunn, 1994; Rapp et al., 1999; Wang et al., 2021) and is stable in the lithospheric mantle at temperatures and pressures up to 1150°C and 3.8 GPa (e.g., Green, 1973; Wallace and Green, 1991; Niida and Green, 1999; Fumagalli et al., 2009; Mandler and Grove, 2016). Under these conditions, particularly within the spinel stability field, amphibole and pyroxene are the main reservoirs of incompatible elements. The trace element contents of pyroxene and amphibole have been used to infer geochemical and petrologic processes that occur in the lithospheric mantle. However, amphibole typically occurs as interstitial grains in mantle rocks. Their small sizes often make trace element analysis challenging, and consequently, concentrations of trace element in amphibole have not been frequently reported alongside those of coexisting pyroxenes (e.g., Liu et al., 2010; Matusiak-Małek et al., 2017; Aradi et al., 2020; Zhang et al., 2022). The objective of the present study is to provide an interim solution to this problem by developing semi-empirical models for the distribution of rare earth elements (REEs) between amphibole and pyroxenes.

In general, partitioning of trace elements between a mineral and its coexisting melt depends on pressure, temperature, and mineral and melt composition. The effects of mineral and melt compositions on REE partitioning between pyroxene and melt and between amphibole and melt have been studied using data from laboratory partitioning

experiments and the lattice strain model (e.g., Klein et al., 1997, 2000; Gaetani et al., 2003; Adam and Green, 2003, 2006; Gaetani, 2004; Sun and Liang, 2012, 2013; Yao et al., 2012; Shimizu et al., 2017). The effects of temperature and mineral composition on REE partitioning between orthopyroxene and clinopyroxene have also been investigated using the lattice strain model (e.g., Stosch, 1982; Hellebrand et al., 2005; Witt-Eickschen and O'Neill, 2005; Lee et al., 2007; Witt-Eickschen et al., 2009; Yao et al., 2012; Liang et al., 2013; Sun and Liang, 2014). Yao et al. (2012), Liang et al. (2013), and Sun and Liang (2014) constructed an orthopyroxene–clinopyroxene REE partitioning model from the pyroxene–melt REE partitioning models. Their model suggested that REE partitioning between the two pyroxenes is sensitive to temperature and pyroxene composition and can be used as a thermometer. For two pyroxene-bearing rocks that experienced cooling, the temperatures derived from the REE-in-two-pyroxene thermometer (Liang et al., 2013) are generally higher than temperatures derived from Ca–Mg–Fe based two-pyroxene thermometers (Wells, 1977; Brey and Köhler, 1990; Putirka, 2008) because REEs diffuse more slowly than major elements in pyroxene (Van Orman et al., 2001, 2002; Dimanov and Wiedenbeck, 2006; Cherniak and Liang, 2007; Müller et al., 2013).

Amphibole has more structural sites and a larger range of chemical compositions than pyroxene (e.g., Leake et al., 1997; Hawthorne et al., 2012). The composition of amphibole varies with physical conditions and compositions of the metasomatic melt and peridotite in the lithospheric mantle (e.g., Niida and Green, 1999; Coltorti et al., 2007; Mandler and Grove, 2016; Wang et al., 2021). Variations in the physical conditions and chemical compositions lead to the difference in compositions between amphibole from the supra-subduction zone (S-amphibole of Coltorti et al., 2007) lithospheric mantle, and

amphibole from the intraplate (I-amphibole of Coltorti et al., 2007) lithospheric mantle. In general, the S-amphibole has a higher Mg# [100 × Mg/(Mg + Fe), atomic ratio] and lower Ti, Na, and K contents than the I-amphibole (Coltorti et al., 2007) (Fig. 1). According to the lattice strain model of Shimizu et al. (2017), amphibole–melt REE partition coefficients increase with increasing Ti and decreasing Na, K, and Mg contents of amphibole.

REE partitioning between pyroxene and amphibole likely depends on physical conditions and mineral compositions. Klein et al. (1997) compared the parameters of the lattice strain model for clinopyroxene–melt REE partitioning with those for amphibole–melt REE partitioning. They concluded that similarities in the Young's moduli and between the M4 site in amphibole and the M2 site in clinopyroxene result in nearly identical clinopyroxene and amphibole REE partition coefficients at given physical conditions, and thus subparallel clinopyroxene and amphibole REE patterns. By comparing the REE contents of coexisting clinopyroxenes and amphiboles in mantle xenoliths from West Eifel, Germany, Witt-Eickschen and O'Neill (2005) inferred that clinopyroxene–amphibole REE partition coefficients are controlled by REE ionic radius and Na content of the clinopyroxene.

Although significant progress has been made in quantifying REE partitioning in amphibole, there is no predictive model for pyroxene–amphibole REE partition coefficients. In this study, we develop temperature- and mineral composition-dependent models for REE partitioning between clinopyroxene, orthopyroxene, and amphibole in mantle rocks. These semi-empirical models are based on lattice strain models of REE partitioning between pyroxene, amphibole, and silicate melt (Sun and Liang, 2012, 2013;

This is the peer-reviewed, final accepted version for American Mineralogist, published by the Mineralogical Society of America.
The published version is subject to change. Cite as Authors (Year) Title. American Mineralogist, in press.
DOI: https://doi.org/10.2138/am-2022-8831. http://www.minsocam.org/

Yao et al., 2012; Shimizu et al., 2017) and are calibrated using natural amphibole-bearing mantle xenoliths. Because amphibole generally crystallized late than pyroxene in the lithospheric mantle, REE partition coefficients obtained from the semi-empirical models are apparent partition coefficients. Nonetheless, the apparent pyroxene–amphibole REE partition coefficients obtained from our models are especially useful for estimating the REE concentrations of amphibole from the REE contents of pyroxene, especially when the grain size of amphibole is too small for trace element analysis.

Theoretical basis

Parameterized mineral–melt REE partitioning models

The theoretical basis of this study is the lattice strain model for partitioning of a REE *i* between a mineral and its coexisting melt (Brice, 1975; Blundy and Wood, 1994; Wood and Blundy, 1997, 2003), which can be written as

$$D_i^{\text{min–melt}} = D_0 \exp\left\{-\frac{4\pi E N_\text{A}}{\text{R}T}\left[\frac{r_0}{2}(r_0 - r_i)^2 - \frac{1}{3}(r_0 - r_i)^3\right]\right\}, \quad (1)$$

where D_0 is the partition coefficient for strain-free substitution; r_0 is the optimum radius for the lattice site; E is the apparent Young's modulus for the lattice site; r_i is the ionic radius of the REE; T is the temperature in K; R is the gas constant; and N_A is Avogadro constant. In general, the lattice parameters D_0, r_0, and E depend on temperature, pressure, and mineral and melt compositions.

Parameterized lattice strain models for amphibole–melt, orthopyroxene–melt, and clinopyroxene–melt REE partitioning were developed by Shimizu et al. (2017), Yao et al. (2012), and Sun and Liang (2012), respectively. These models show that mineral–melt REE partition coefficients depend on temperature and mineral chemistry. With decreasing

temperature, mineral–melt REE partition coefficients increase. In the amphibole model of Shimizu et al. (2017), D_0 is positively correlated with Ti in amphibole but negatively corelated with Mg, Na, and K in amphibole, r_0 is negatively correlated with the ferromagnesian content of the M4 site in amphibole ($X_{\mathrm{Fm}}^{\mathrm{M4}}$); and E is a constant. In the low-Ca pyroxene model of Yao et al. (2012), D_0 is positively corelated with Ca content of the M2 site ($X_{\mathrm{Ca}}^{\mathrm{M2}}$) and Al content of the tetrahedral site ($X_{\mathrm{Al}}^{\mathrm{T}}$) in the pyroxene, and in the clinopyroxene model of Sun and Liang (2012), D_0 is positively correlated with $X_{\mathrm{Al}}^{\mathrm{T}}$ and Mg content of the M2 site ($X_{\mathrm{Mg}}^{\mathrm{M2}}$) in the pyroxene. r_0 and E in the two pyroxene models also depend on pyroxene composition. The lattice strain parameters of the three mineral–melt REE partitioning models are summarized in Appendix A.

The amphiboles used to calibrate the partitioning model of Shimizu et al. (2017) were produced at 780–1100°C and 0.2–2.5 GPa through laboratory experiments. Oxygen fugacities of these experiments are -2 to +3.2 logarithmic unit from the quartz-fayalite-magnetite buffer, which covers a large range of those calculated for spinel peridotite from different tectonic settings (Frost and McCammon, 2008). The experimental amphiboles contain 0.73–6.35 wt% TiO_2, 1.20–4.04 wt% Na_2O, and 0.03–2.77 wt% K_2O, and have Mg#s ranging from 36 to 100 (Fig. 1). Their compositions overlap with a majority (81%) of I-amphiboles but only a small portion (15%) of S-amphiboles from mantle rocks reported in the literature. The latter have lower TiO_2 and Na_2O, but higher SiO_2 and Mg# than amphiboles from the partitioning experiments (Figs. 1a–1c). The Mg#s of clinopyroxenes and low-Ca pyroxenes from the partitioning experiments for calibrating the parameterized models of Sun and Liang (2012, 2013) and Yao et al. (2012) are 54–100 and 70–100, respectively, covering the main range of

This is the peer-reviewed, final accepted version for American Mineralogist, published by the Mineralogical Society of America.
The published version is subject to change. Cite as Authors (Year) Title. American Mineralogist, in press.
DOI: https://doi.org/10.2138/am-2022-8831. http://www.minsocam.org/

pyroxene compositions in mantle rocks.

Pyroxene–amphibole REE partitioning models

When two minerals (α and β) and the melt are in thermodynamic equilibrium, it is possible to calculate the mineral–mineral REE partition coefficients by taking the ratio of the two mineral–melt partition coefficients, viz.,

$$D_i^{\beta-\alpha} = \frac{D_i^{\beta\text{-melt}}}{D_i^{\alpha\text{-melt}}} = \frac{D_0^{\beta}}{D_0^{\alpha}} \exp\left\{ \begin{array}{l} -\frac{4\pi E^{\beta} N_A}{RT}\left[\frac{r_0^{\beta}}{2}\left(r_0^{\beta}-r_i\right)^2 - \frac{1}{3}\left(r_0^{\beta}-r_i\right)^3\right] \\ +\frac{4\pi E^{\alpha} N_A}{RT}\left[\frac{r_0^{\alpha}}{2}(r_0^{\alpha}-r_i)^2 - \frac{1}{3}(r_0^{\alpha}-r_i)^3\right] \end{array} \right\}. \quad (2)$$

Yao et al. (2012), Liang et al. (2013), and Sun and Liang (2014) demonstrated that Eq. (2) reproduces the measured orthopyroxene–clinopyroxene REE partition coefficients in well-equilibrated peridotites and can be used under magmatic and subsolidus conditions. The REE-in-two-pyroxene thermometer of Liang et al. (2013) was developed by rearranging Eq. (2). Temperatures obtained from the REE thermometer (T_{REE}) for well-equilibrated peridotites are similar to those obtained from major element-based pyroxene thermometers such as those of Brey and Köhler (1990), Wells (1977), and Putirka (2008) (gray fields in Fig. 2).

Applying Eq. (2) to the mineral pairs of pyroxene and amphibole, we have the orthopyroxene–amphibole and clinopyroxene–amphibole REE partitioning models:

$$D_i^{\text{pyx-amp}} = \frac{D_i^{\text{pyx-melt}}}{D_i^{\text{amp-melt}}} = \frac{D_0^{\text{pyx}}}{D_0^{\text{amp}}} \exp\left\{ \begin{array}{l} -\frac{4\pi E^{\text{pyx}} N_A}{RT}\left[\frac{r_0^{\text{pyx}}}{2}\left(r_0^{\text{opx}}-r_i\right)^2 - \frac{1}{3}\left(r_0^{\text{pyx}}-r_i\right)^3\right] \\ +\frac{4\pi E^{\text{amp}} N_A}{RT}\left[\frac{r_0^{\text{amp}}}{2}\left(r_0^{\text{amp}}-r_i\right)^2 - \frac{1}{3}\left(r_0^{\text{amp}}-r_i\right)^3\right] \end{array} \right\}, \quad (3)$$

where pyx is either orthopyroxene (opx) or clinopyroxene (cpx), and the lattice strain parameters are presented in Appendix A. Eq. (3) is valid so long as pyroxene and

amphibole are in chemical equilibrium.

Major element and REE data of pyroxenes and amphibole in amphibole-bearing mantle rocks from the literature can be used to test the pyroxene-amphibole REE partitioning models (e.g., Gregoire et al., 2000; Witt-Eickschen and O'Neill, 2005; Ishimaru et al., 2007; Xu et al., 2010; Bénard et al., 2013, 2021; Zhou, 2014; Pintér et al., 2015; Matusiak-Małek et al., 2017; Aradi et al., 2020; Belousov et al., 2021; Nishio et al., 2022). In order to apply these models, a mantle sample must meet the following two requirements: (1) amphibole and pyroxene compositions are within the calibration ranges of the mineral–melt partitioning models, and (2) amphibole and pyroxenes crystallized from the same melt, i.e., formed from the same metasomatic event. The calibration ranges of pyroxene-melt partitioning models of Sun and Liang (2012, 2013) and Yao et al. (2012) cover pyroxene compositions of mantle rocks, including the collected amphibole-bearing samples. Twenty-eight of the amphibole-bearing mantle rocks from the literature cited above have amphibole compositions within the calibration range of amphibole–melt partitioning model of Shimizu et al. (2017). They include 26 samples with I-amphibole from Western Pannonian Basin, Hungary (Aradi et al., 2020), Nyos Lakes, Cameroon (Pinter et al., 2015), Wilcza Góra, Southwestern Poland (Matusiak-Malek et al., 2017), Huadian, northeastern China (Xu, unpublished), and 2 samples with S-amphibole from Laiwu, North China Craton (Zhou, 2014). To check if requirement (2) is met, we examined the texture and mineral chemistry for the 28 samples (See Text S1 of online Appendix C for details.) Among these samples, 2 peridotites with I-amphibole from Western Pannonian Basin and the 2 websterites with S-amphibole from Laiwu show significant disequilibrium textures. Additionally, their constituent pyroxenes have

This is the peer-reviewed, final accepted version for American Mineralogist, published by the Mineralogical Society of America.
The published version is subject to change. Cite as Authors (Year) Title. American Mineralogist, in press.
DOI: https://doi.org/10.2138/am-2022-8831. http://www.minsocam.org/

204 significantly higher Mg#s (by 3.5–8.1 unites) than amphibole Mg#s (Fig. 3a, Table S1).
205 These samples are excluded from the test. The remaining 24 samples all contain
206 I-amphibole. Their orthopyroxene Mg#s are similar to the clinopyroxene Mg#s, but both
207 pyroxene Mg#s are slightly higher (by 1.0–3.0 units) than amphibole Mg# (Fig. 3b, Table
208 S1). Figure 2 compares the temperatures calculated using the REE-in-two-pyroxene
209 thermometer (T_{REE}, Liang et al., 2013) with those calculated using the major-element
210 based two-pyroxene thermometers of Brey and Köhler (1990, T_{BKN}), Wells (1977, T_{W77}),
211 Putirka (2008, his Eq. (37), T_{P37}), and average of the three temperatures (T_{avg}) for the 24
212 amphibole-bearing mantle rocks. Temperatures of these samples are mostly within the
213 range of well-equilibrated mantle xenoliths, suggesting that the REEs (at least the heavy
214 REEs) and major elements in orthopyroxene are in equilibrium with those in
215 clinopyroxene (Liang et al., 2013).

216 Figure 4a shows the inversion diagram based on the REE-in-two-pyroxene
217 thermometer of Liang et al. (2013) for an amphibole-bearing lherzolite from Wilcza Góra,
218 SW Poland (Matusiak-Malek et al., 2017, sample WLK30). Using the inverted
219 temperature (T_{REE} = 1010 ± 14°C), the mineral–mineral REE partitioning model of Eq. (2)
220 well reproduced orthopyroxene–clinopyroxene partition coefficients for most of the REEs
221 (Fig. 4b). The exceptions are La and Ce, which may be attributed to their higher closure
222 temperatures (Liang, 2015). Interestingly, the pyroxene–amphibole REE partition
223 coefficients calculated using Eq. (3), T_{REE}, and major element compositions of the
224 amphibole and pyroxenes differ markedly from the measured values (Fig. 4c and 4d). The
225 isotherms established by the orthopyroxene–amphibole REE partitioning model indicate
226 that orthopyroxene and amphibole would be equilibrated at a lower temperature (between

This is the peer-reviewed, final accepted version for American Mineralogist, published by the Mineralogical Society of America.
The published version is subject to change. Cite as Authors (Year) Title. American Mineralogist, in press.
DOI: https://doi.org/10.2138/am-2022-8831. http://www.minsocam.org/

750°C and 925°C, Fig. 4c). In addition, the model-derived clinopyroxene–amphibole REE partition coefficients are well above the measured values, suggesting REEs in amphibole and clinopyroxene are not in equilibrium at any temperature (Fig. 4d). A likely explanation is that amphibole crystallized at a temperature lower than T_{REE}, and that chemical equilibria between amphibole and the pyroxenes have not been established. This is consistent with the observation from hydrous melt–peridotite reactive crystallization experiments of Wang et al. (2021), where the interstitial and overgrowth occurrences of amphibole in the product peridotite and pyroxenite suggest a later crystallization of amphibole than pyroxenes. Below, we present a semi-empirical model that can be used to estimate the crystallization temperature of amphibole in mantle rocks.

Semi-empirical models for crystallization temperature of amphibole

Since the amphibole crystallizes later than the pyroxenes, the pyroxene–melt and amphibole–melt REE partition coefficients are defined at their crystallization temperatures (T^{pyx} and T^{amp}, respectively). Taking the ratio of $D^{pyx-melt}$ at T^{pyx} and $D^{amp-melt}$ at T^{amp}, we have, from the lattice strain model (Eq. (1)), the pyroxene-amphibole apparent partition coefficient:

$$D_i^{\mathrm{pyx\text{-}amp}} = \frac{C_i^{\mathrm{pyx}}}{C_i^{\mathrm{amp}}} = \frac{D_i^{\mathrm{pyx\text{-}melt_{pyx}}} C_i^{\mathrm{melt_{pyx}}}}{D_i^{\mathrm{amp\text{-}melt_{amp}}} C_i^{\mathrm{melt_{amp}}}}$$

$$= \frac{D_0^{\mathrm{pyx}}}{D_0^{\mathrm{amp}}} \exp\left\{ \begin{array}{c} -\frac{4\pi E^{\mathrm{pyx}} N_A}{\mathrm{R}T^{\mathrm{pyx}}}\left[\frac{r_0^{\mathrm{pyx}}}{2}\left(r_0^{\mathrm{pyx}} - r_i\right)^2 - \frac{1}{3}\left(r_0^{\mathrm{pyx}} - r_i\right)^3\right] \\ +\frac{4\pi E^{\mathrm{amp}} N_A}{\mathrm{R}T^{\mathrm{amp}}}\left[\frac{r_0^{\mathrm{amp}}}{2}\left(r_0^{\mathrm{amp}} - r_i\right)^2 - \frac{1}{3}\left(r_0^{\mathrm{amp}} - r_i\right)^3\right] \\ +\ln\frac{C_i^{\mathrm{melt_{pyx}}}}{C_i^{\mathrm{melt_{amp}}}} \end{array} \right\}, \quad (4)$$

where $\mathrm{melt_{pyx}}$ and $\mathrm{melt_{amp}}$ are melts in equilibrium with pyroxene and amphibole,

This is the peer-reviewed, final accepted version for American Mineralogist, published by the Mineralogical Society of America.
The published version is subject to change. Cite as Authors (Year) Title. American Mineralogist, in press.
DOI: https://doi.org/10.2138/am-2022-8831. http://www.minsocam.org/

respectively, and $\frac{C_i^{\mathrm{melt_{pyx}}}}{C_i^{\mathrm{melt_{amp}}}}$ is the ratio of melt REE concentrations at the two equilibrium temperatures. Given the generally small amount of amphibole crystallized after pyroxenes in the mantle samples and the moderate incompatibility of REEs in amphibole (partition coefficients mostly 0.1–1) at a range of temperatures (780–1100°C) (Shimizu et al., 2017), we infer that the ratio $\frac{C_i^{\mathrm{melt_{pyx}}}}{C_i^{\mathrm{melt_{amp}}}}$ is on the order of one, and thus $\ln\frac{C_i^{\mathrm{melt_{pyx}}}}{C_i^{\mathrm{melt_{amp}}}}$ is negligible compared to contributions from lattice strains in pyroxenes and amphibole. Hence, Eq. (4) can be simplified as:

$$D_i^{\mathrm{pyx-amp}} = \frac{D_0^{\mathrm{pyx}}}{D_0^{\mathrm{amp}}} \exp\left\{ \begin{array}{l} -\frac{4\pi E^{\mathrm{pyx}} N_A}{\mathrm{R}T^{\mathrm{pyx}}}\left[\frac{r_0^{\mathrm{pyx}}}{2}\left(r_0^{\mathrm{pyx}} - r_i\right)^2 - \frac{1}{3}\left(r_0^{\mathrm{pyx}} - r_i\right)^3\right] \\ +\frac{4\pi E^{\mathrm{amp}} N_A}{\mathrm{R}T^{\mathrm{amp}}}\left[\frac{r_0^{\mathrm{amp}}}{2}\left(r_0^{\mathrm{amp}} - r_i\right)^2 - \frac{1}{3}\left(r_0^{\mathrm{amp}} - r_i\right)^3\right] \end{array} \right\}, \quad (5)$$

where T^{amp} is the apparent amphibole–melt REE partitioning temperature or amphibole crystallization temperature while neglecting the difference in melt REE concentration ($\ln\frac{C_i^{\mathrm{melt_{pyx}}}}{C_i^{\mathrm{melt_{amp}}}}$ in Eq. (4)). Rearranging Eq. (5), we have

$$\ln D_i^{\mathrm{pyx-amp}} = A_i^{\mathrm{pyx,amp}} + \frac{B_i^{\mathrm{amp}}}{T^{\mathrm{amp}}}. \quad (6)$$

The terms $A_i^{\mathrm{pyx,amp}}$ and B_i^{amp} are presented in Appendix B. Eq. (6) can be written in the linear form:

$$B_i^{\mathrm{amp}} = T^{\mathrm{amp}}\left(\ln D_i^{\mathrm{pyx-amp}} - A_i^{\mathrm{pyx,amp}}\right). \quad (7)$$

In the absence of additional information, we can approximate T^{pyx} using the temperature derived from the REE-in-two-pyroxene thermometer of Liang et al. (2013, T_{REE}). The apparent amphibole temperature can be calculated using an inversion diagram constructed by plotting $\left(\ln D_i^{\mathrm{opx-amp}} - A_i^{\mathrm{opx,amp}}\right)$ or $\left(\ln D_i^{\mathrm{cpx-amp}} - A_i^{\mathrm{cpx,amp}}\right)$ against

This is the peer-reviewed, final accepted version for American Mineralogist, published by the Mineralogical Society of America.
The published version is subject to change. Cite as Authors (Year) Title. American Mineralogist, in press.
DOI: https://doi.org/10.2138/am-2022-8831. http://www.minsocam.org/

265 B_i^{amp}. The slope of regression line passing through the origin in the diagram is the
266 apparent temperature.

267 Figures 5a and 5b display the inversion diagrams of the apparent amphibole
268 temperatures for the amphibole-bearing lherzolite shown in Fig. 4 (sample WLK30 from
269 Matusiak-Malek et al., 2017). Using the robust linear least-squares regression method, we
270 fit a line through the origin and data in the diagram, and obtain the temperature from the
271 slope of this line. Similar apparent temperatures are obtained from the orthopyroxene–
272 amphibole REE partitioning data ($T^{\mathrm{amp,opx–amp}}$ = 856 ± 10°C) and the clinopyroxene–
273 amphibole REE partitioning data ($T^{\mathrm{amp,cpx–amp}}$ = 861 ± 5°C). In Figures S1–S24 of online
274 Appendix C, we present the T^{amp} inversion diagrams for the 24 mantle samples included
275 in this study. For most of the samples, data of light and some middle REEs are off the
276 regression line, and these outliers were excluded from the inversion. Most of these
277 elements are also outliers in the inversion diagrams when applying the
278 REE-in-two-pyroxene thermometer of Liang et al. (2013). This is attributed in part to the
279 low analytical precision for the depleted light REEs (Liang et al., 2013) and their higher
280 closure temperatures (Liang, 2015). Substituting the inverted amphibole temperature
281 (856°C or 861°C) and T_{REE} (1010°C) into Eq. (5), we obtain orthopyroxene–amphibole
282 and clinopyroxene–amphibole REE partition coefficients. These partition coefficients
283 reproduce the measured values for sample WLK30 (Figs. 5c and 5d). The inverted
284 amphibole temperatures for the amphibole-bearing mantle xenoliths range from 754°C to
285 959°C, which are 69–205°C lower than T_{REE}s (Figs. S1–S24). The amphibole
286 temperatures inverted from the orthopyroxene–amphibole model ($T^{\mathrm{amp,opx–amp}}$) and those
287 from the clinopyroxene–amphibole modal ($T^{\mathrm{amp,cpx–amp}}$) are generally in agreement with

This is the peer-reviewed, final accepted version for American Mineralogist, published by the Mineralogical Society of America.
The published version is subject to change. Cite as Authors (Year) Title. American Mineralogist, in press.
DOI: https://doi.org/10.2138/am-2022-8831. http://www.minsocam.org/

each other (Figs. S1-S24), suggesting the internal consistency of our semi-empirical models.

Partition coefficients of REE between pyroxene and amphibole

T-*X*-dependent pyroxene-amphibole REE partition coefficients

To predict pyroxene-amphibole partition coefficients through temperature (T) and mineral major element composition (X), we need the amphibole crystallization temperature (T^{amp}) without relying on its REE data. For this purpose, we fit the inverted T^{amp} (average value of $T^{amp,opx-amp}$ and $T^{amp,cpx-amp}$) with amphibole major element compositions for the 24 samples using the least squares method, and obtain the empirical expression:

$$T^{amp}(°C) = 258(\pm33)X_{Si} + 822(\pm134)X_{Ti} - 743(\pm208)X_{Na} - 507(\pm213)X_{K} + 755(\pm131)X_{Fm}^{M4} - 273.15. \quad (8)$$

The amphibole components are calculated using the method of Shimizu et al. (2017) which is described in Text S2 of online Appendix C. Numbers in parentheses are standard error of the coefficients. We also attempted to include pyroxene components in the regression, such as Al, Mg, Ca, and Na. The prediction is not significantly improved, and large uncertainties are introduced. T^{amp} calculated using Eq. (8) is generally within ±50°C deviation from the T^{amp} inverted using the partitioning models of Eq. (7) (Fig. 6a). The calculated T^{amp} are commonly lower than temperatures calculated from the two-pyroxene thermometers (T_{REE}, T_{BKN}, T_{W77}, and T_{P37}, Figs. 6b-6f). The empirical Eq. (8) for T^{amp} allows us to predict $D^{opx-amp}$ and $D^{cpx-amp}$ for amphibole-bearing mantle samples using Eq. (5).

311 Figure 7 compares the predicted pyroxene–amphibole REE partition coefficients
312 with measured values for the amphibole-bearing mantle rocks. T^{amp} in the models is
313 calculated using Eq. (8). The models are capable of reproducing the partition coefficients
314 of Dy–Lu and Y. The orthopyroxene–amphibole model underestimates some of the La–
315 Tb partition coefficients (Fig. 7a and 7b). Out of 341 orthopyroxene-amphibole REE
316 partition coefficients, seventy-eight (mostly La–Sm) plot below the 1:2 correlation line
317 (Fig. 7a). These outliers are also the outliers on the inversion diagrams for T_{REE} and T^{amp}
318 (Figures S1-S24). The clinopyroxene–amphibole model does a better job for reproducing
319 REE partition coefficients for the mantle samples than the orthopyroxene–amphibole
320 model (Figs. 7c and 7d). Out of 356 orthopyroxene-amphibole REE partition coefficients,
321 twenty (mostly La–Nd) plot above the 2:1 correlation line, and 94% of the data plot
322 between the 1:2 and 2:1 correlation lines (Fig. 7c).
323
324 **Effect of amphibole crystallization temperature**
325 We have demonstrated that, in the pyroxene-amphibole REE partitioning models, the
326 amphibole temperature (T^{amp}) is generally lower than T^{pyx} (Fig. 6). To test the effect of
327 amphibole crystallization temperature on pyroxene–amphibole REE partitioning, we
328 calculated pyroxene–amphibole REE partition coefficients for the lherzolite from Wilcza
329 Góra (Matusiak-Małek et al., 2017, sample WLK30) and a lherzolite from the Western
330 Pannonian Basin, Hungary (Aradi et al., 2020, sample AUB1407), using the models
331 presented above and assuming T^{amp}s that are 50–300°C lower than T^{pyx} (assigned as T_{REE}).
332 Although major element compositions and modal mineral abundances vary during
333 cooling, no model is available to account for these changes, and we neglected these

variations for the purpose of this exercise. As shown in Fig. 8, the calculated pyroxene–amphibole REE partition coefficients decrease systematically with increasing deviation of T^{amp} from T^{pyx}. This is attributed to the negative correlation of amphibole–melt REE partition coefficients with temperature (Shimizu et al., 2017). In addition, with increasing deviation of T^{amp} from T^{pyx}, the pyroxene-amphibole mid REE partition coefficients decrease more dramatically than heavy and light REE partition coefficients. Since amphibole generally crystallizes after pyroxenes during hydrous melt–peridotite reactions (e.g., Wang et al., 2021), the preceding exercise underscores the importance of crystallization sequence on the REE distributions between pyroxenes and amphibole.

Field applications

Conditions of application and a program for calculation

The semi-empirical partitioning models presented in the preceding sections (Eqs. (5)-(8)) can be used to calculate apparent pyroxene–amphibole REE partition coefficients for amphibole-bearing mantle rocks that have mineral compositions comparable to those from experiments used to calibrate the mineral–melt REE partitioning models (Sun and Liang, 2012, 2013; Yao et al., 2013; Shimizu et al., 2017). The pyroxene–melt models cover the main range of pyroxene compositions in mantle rocks, whereas the amphibole–melt model covers mostly the I-amphiboles (Fig. 1). Hence it is important to check amphibole chemistry before an application. Another caveat is that the constituent amphibole and pyroxenes were formed or affected by the same metasomatic event. This can be assessed from texture and mineral composition (e.g., Mg#s). As we have shown in Fig. 2b, the amphibole Mg# is slightly lower than the pyroxene Mg#s, and the differences

between pyroxene Mg#s and amphibole Mg# in samples for calibration are less than 3 units.

In the online Appendix D, we provide an Excel worksheet that can be used to calculate pyroxene-amphibole REE partition coefficients for amphibole-bearing mantle rocks. It requires inputs of pyroxene and amphibole major element compositions and T^{pyx}. The pyroxene temperature can be estimated using the REE-in-two-pyroxene thermometer of Liang et al. (2013). For mantle rocks from well-equilibrated lithospheric mantle, major element-derived temperatures are similar to T_{REE} (Fig. 2). Temperatures calculated using pyroxene thermometers such as T_{BKN}, T_{p37}, and T_{w77} can also be used as T^{pyx} when T_{REE} is inaccessible.

Applications

To test and validate the pyroxene–amphibole REE partitioning models, we calculate the REE contents of amphibole-bearing mantle xenoliths and compare them with the measured amphibole REE contents. The harzburgite xenoliths WG5 and WG6 from Wilcza Góra, Poland (Matusiak-Małek et al., 2017), consist of coarse grains of olivine, orthopyroxene (± clinopyroxene), and fine-grained intergranular aggregates. The aggregates contain secondary amphibole and clinopyroxene (± phlogopite). Matusiak-Małek et al. (2017) reported major element and REE compositions of the orthopyroxenes for WG5, clinopyroxenes for WG6, and major element compositions of amphiboles for both samples. Mg#s in pyroxene and amphibole are similar (91 in orthopyroxene and 89 in amphibole for WG5, and 88 in clinopyroxene and 85 in amphibole for WG6). They calculated pyroxene temperatures using the

Al-in-orthopyroxene thermometer of Witt-Eickschen and Seck (1991) for WG5 (990°C) and the REE-in-two-pyroxene thermometer of Liang et al. (2013) for WG6 (1023°C). Using the available data and our models, we obtained T^{amp}s for WG5 (888°C) and WG6 (852°C), and calculated pyroxene–amphibole REE partition coefficients and REE contents of the amphiboles. The chondrite-normalized REE patterns are presented in Fig. 9a. The calculated amphibole REE patterns of samples WG5 and WG6 are similar to those of the genetically related samples (Matusiak-Małek et al., 2017). The predicted REE contents of the amphibole in WG5 are higher than those of the other samples, and the predicted REE pattern for the amphibole in WG6 shows less fractionation between light and heavy REEs than those of the other samples (pink field in Fig. 8a, Matusiak-Małek et al., 2017). These are consistent with differences in the REE patterns of the pyroxene in WG5 and WG6, and in the other samples (Figures 6c and 7e in Matusiak-Małek et al., 2017).

Another set of examples are the lherzolite xenoliths KPFS0402 and PST1403 from the Western Pannonian Basin, Hungary (Aradi et al., 2020). KPFS0402 has a protogranular texture and contains 0.2% amphibole, and PST1403 has a porphyroclastic texture with 0.02% amphibole. The amphibole crystals in both xenoliths grew on the rims of clinopyroxene and spinel grains. The two samples have uniform orthopyroxene, clinopyroxene, and amphibole Mg#s (90/89/88 and 91/91/89). Using the reported mineral compositional data, we calculated T_{REE} (1025°C and 1018°C) and T^{amp} (927°C and 929°C) for the two samples, as well as the pyroxene–amphibole REE partition coefficients. The REE contents of amphibole in the two samples calculated using the partition coefficients and the measured clinopyroxene and orthopyroxene REE data are plotted in Fig. 9b. The

amphibole REE patterns are comparable to measured patterns of amphiboles in xenoliths that have similar petrologic features and sample locations (green field in Fig. 8b, Aradi et al., 2020). Amphibole REE patterns calculated from orthopyroxene–amphibole partitioning are perturbed for REEs from La to Gd. This perturbation is in correspondence with those in the orthopyroxene REE patterns (Aradi et al., 2020), which is likely a result of the low concentrations of the light to middle REEs in orthopyroxene relative to the analytical precision.

Recently, Puziewicz et al. (2023) reported two amphibole-bearing lherzolites from Cameroon volcanic line. Sample H71 has a porphyroclastic texture, and small amphiboles (1%) are dispersed among olivine and pyroxene grains. It has similar T_{REE} (901°C) and T_{BKN} (911°C). Orthopyroxene, clinopyroxene, and amphibole have similar Mg#s (90, 92, and 89). Using the reported mineral major element data and T_{REE}, we calculated T^{amp} (778°C) and pyroxene–amphibole REE partition coefficients. The predicted REE patterns are compared with the measured pattern in Fig. 9c. The models mimic middle to heavy REE pattern of the amphibole, but slightly overestimate concentrations of light REEs. The elevated La, Ce, and Pr in amphibole follow that of orthopyroxene REEs.

The other Cameroon lherzolite (sample H69 from Puziewicz et al., 2023) has a sheared texture, and contains more abundant amphibole (3.9%). The amphibole forms asymmetric aggregates around spinels and unevenly distributed in the sample. T_{BKN} (952°C) of this sample is considerably higher than T_{REE} (872°C), which suggests a possible heating event after the formation of pyroxenes. T^{amp} obtained from Eq. (8) are 652°C. Our models overestimate amphibole REE contents, even for the heavy REEs (Fig.9d). This suggests that Eq. (8) is not capable of estimating amphibole temperature

426 from compositions of pyroxene and amphibole that experienced heating. T^{amp} is likely
427 higher than the calculated values since $D^{pyx\text{-}amp}$s increase with decreasing difference
428 between T^{pyx} and T^{amp} (Fig. 8). This can be testified by the T^{amp} inverted using the REE
429 partitioning models of Eq. (7). Both the orthopyroxene-amphibole and
430 clinopyroxene-amphibole models yield an T^{amp} of 745°C (Fig. 9d).
431

432 **Summary**

433 Based on the parameterized lattice strain models for pyroxene–melt and amphibole–
434 melt REE partitioning (Sun and Liang, 2012, 2013; Yao et al., 2012; Shimizu et al., 2017),
435 we developed semi-empirical models for REE partitioning between orthopyroxene and
436 amphibole and between clinopyroxene and amphibole. The models were calibrated using
437 24 amphibole-bearing mantle samples that have major element and REE compositions of
438 pyroxenes and amphibole reported in the literature. These amphibole-bearing mantle
439 rocks have similar REE-derived temperatures (Liang et al., 2013) and major
440 element-derived two-pyroxene temperatures (e.g., Wells, 1977; Brey and Köhler, 1990;
441 Putirka, 2008). However, the mineral–melt REE partitioning models indicate that the
442 amphibole–melt equilibrium temperatures are generally lower than the two-pyroxene
443 temperatures, supporting the experimental observation that amphibole crystallizes later
444 than pyroxene during hydrous melt–peridotite reaction (e.g., Wang et al., 2021).
445 Therefore, we use the term "apparent temperature" for the amphibole–melt equilibrium
446 temperature, and empirically regressed the apparent temperature against amphibole major
447 element compositions (Eq. (8)). The partitioning models (Eq. (5)), combined with the
448 empirical model for the apparent temperature, can be used to predict orthopyroxene–

449 amphibole and clinopyroxene–amphibole REE partition coefficients for mantle rocks
450 containing I-amphibole (Coltorti et al., 2007).
451

452 ## Implications

453 The temperature- and composition-dependent REE partitioning models presented in
454 this study make it possible to estimate REE concentrations in amphibole in mantle rocks
455 using REE contents of coexisting orthopyroxene or clinopyroxene. The new partitioning
456 models require major element compositions of amphibole and pyroxenes and the
457 temperature at which the pyroxenes equilibrated. This temperature can be obtained from
458 pyroxene thermometers, including those of Wells (1977), Brey and Köhler (1990),
459 Putirka (2008), and Liang et al. (2013).

460 The amphibole crystallization temperature has been quantified using thermometers
461 based on amphibole composition, the coexisting melt composition, or a combination of
462 the two (e.g., Ridolfi and Renzulli, 2012; Molina et al., 2015; Putirka, 2016). However,
463 these thermometers were not designed for mantle rocks. The REE partitioning models
464 (Eq. (7)) or the empirical Eq. (8) can be used to invert or calculate amphibole
465 crystallization temperature. Hence, the semi-empirical and empirical models for
466 amphibole crystallization temperature presented in this study have potential implications
467 for constraining the thermal property of the amphibole-bearing lithospheric mantle.
468

469 ## Acknowledgements

470 We wish to thank Federico Casetta and Chun-Ming Wu for their detailed comments
471 and constructive suggestions which helped to improve this manuscript. We also thank

Julie Roberge for the editorial handling. This work was supported by grants from National Natural Science Foundation of China (42072072), US National Science Foundation (EAR-2147598), and a Program for JLU Science and Technology Innovative Research Team (2021TD-05).

Appendix A. Parameters in the lattice strain models for REE partitioning between amphibole, pyroxenes and silicate melts

The following equations summarize the parameters used in the lattice strain models for REE partitioning between mantle minerals (amphibole, clinopyroxene, and low-Ca pyroxene) and silicate melts of Eq. (3):

Amphibole model (Shimizu et al., 2017)

$$\ln D_0 = -4.21 + \frac{7.27\times10^4}{RT} + 1.52X_{\mathrm{Ti}} - 0.35X_{\mathrm{Mg}} - 1.83X_{\mathrm{Na}} - 2.95X_{\mathrm{K}}, \quad \text{(A1a)}$$

$$r_0(\text{Å}) = 1.043 - 0.039X_{\mathrm{Fm}}^{\mathrm{M4}}, \quad \text{(A1b)}$$

$$E(\mathrm{GPa}) = 337. \quad \text{(A1c)}$$

Clinopyroxene model (Sun and Liang, 2012)

$$\ln D_0 = -7.14 + \frac{7.19\times10^4}{\mathrm{R}T} + 4.37X_{\mathrm{Al}}^{\mathrm{T}} + 1.98X_{\mathrm{Mg}}^{\mathrm{M2}} - 0.91X_{\mathrm{H_2O}}^{\mathrm{melt}}, \quad \text{(A2a)}$$

$$r_0(\text{Å}) = 1.066 - 0.104X_{\mathrm{Al}}^{M1} - 0.212X_{\mathrm{Mg}}^{\mathrm{M2}}, \quad \text{(A2b)}$$

$$E(\mathrm{GPa}) = (2.27r_0 - 2.00)\times10^3. \quad \text{(A2c)}$$

Low-Ca pyroxene model (Yao et al., 2012; Sun and Liang, 2013)

$$\ln D_0 = -5.37 + \frac{3.87\times10^4}{\mathrm{R}T} + 3.54X_{\mathrm{Al}}^{\mathrm{T}} + 3.56X_{\mathrm{Ca}}^{\mathrm{M2}} - 0.84X_{\mathrm{Ti}}^{\mathrm{melt}}, \quad \text{(A3a)}$$

$$r_0(\text{Å}) = 0.693 + 0.432X_{\mathrm{Ca}}^{\mathrm{M2}} + 0.228X_{\mathrm{Mg}}^{\mathrm{M2}}, \quad \text{(A3b)}$$

$$E(\mathrm{GPa}) = (1.85r_0 - 1.37 - 0.53X_{\mathrm{Ca}}^{\mathrm{M2}})\times10^3. \quad \text{(A3c)}$$

This is the peer-reviewed, final accepted version for American Mineralogist, published by the Mineralogical Society of America.
The published version is subject to change. Cite as Authors (Year) Title. American Mineralogist, in press.
DOI: https://doi.org/10.2138/am-2022-8831. http://www.minsocam.org/

494 In Eqs. (A1a) and (A1b), X_{Ti}, X_{Mg}, X_{Na}, and X_{K} are cation numbers of Ti, Mg, Na,
495 and K per 23-oxygen, and $X_{\mathrm{Fm}}^{\mathrm{M4}}$ is the total cation number of Fe^{2+} + Mn^{2+} + Mg^{2+} on the
496 M4 site. The amphibole formula is calculated using the method described in Shimizu et al.
497 (2017). This method is simplified from that in Leake et al. (1997) by assuming all Fe to
498 be ferrous for parameterizing the amphibole-melt REE partitioning model. The
499 calculation procedure is described in Text S2 of online Appendix C. In Eqs. (A2a), (A2b),
500 and (A3a–c), $X_{\mathrm{Al}}^{\mathrm{T}}$ is the cation content of the tetrahedral Al in pyroxene per 6-oxygen;
501 $X_{\mathrm{Al}}^{\mathrm{M1}}$ is the cation number of Al on the M1 site in pyroxene per 6 oxygen; $X_{\mathrm{Ca}}^{\mathrm{M2}}$ and $X_{\mathrm{Mg}}^{\mathrm{M2}}$
502 are cation numbers of Ca and Mg, respectively, on the M2 site in pyroxene per 6 oxygen;
503 $X_{\mathrm{H_2O}}^{\mathrm{melt}}$ is the molar fraction of H_2O in the melt calculated following Wood and Blundy
504 (2002); and $X_{\mathrm{Ti}}^{\mathrm{melt}}$ is the cation fraction of Ti in the melt per 6 oxygen. $X_{\mathrm{Ti}}^{\mathrm{melt}}$ is added
505 to correct the effect of melt TiO_2 for REE partitioning between low-Ca pyroxene and
506 lunar basalts which have high TiO_2 concentrations, and it can be neglect in cases of
507 Earth's mantle conditions (Yao et al., 2012; Sun and Liang, 2013). Pyroxene formulae are
508 calculated by assuming a random distribution of Fe^{2+} and Mg^{2+} over the M1 and M2 sites
509 (Wood and Banno, 1973) and that all iron is present as ferrous iron (Sun and Liang, 2012,
510 2013; Yao et al., 2012).
511

512 **Appendix B. Parameters in the semi-empirical models for amphibole temperature**

513 The following equations present the expressions of terms and in the semi-empirical
514 models for amphibole temperature of (Eq. (5)):

515 $$A_i^{\mathrm{opx,amp}} = -5.37 + \frac{3.87\times10^4}{RT^{\mathrm{pyx}}} + 3.54X_{\mathrm{Al}}^{\mathrm{T,opx}} + 3.56X_{\mathrm{Ca}}^{\mathrm{M2,opx}} + 4.21 - 1.52X_{\mathrm{Ti}}^{\mathrm{amp}} +$$

This is the peer-reviewed, final accepted version for American Mineralogist, published by the Mineralogical Society of America.
The published version is subject to change. Cite as Authors (Year) Title. American Mineralogist, in press.
DOI: https://doi.org/10.2138/am-2022-8831. http://www.minsocam.org/

$$0.35X_{\mathrm{Mg}}^{\mathrm{amp}} + 1.83X_{\mathrm{Na}}^{\mathrm{amp}} + 2.95X_{\mathrm{K}}^{\mathrm{amp}} - \frac{4\pi E^{\mathrm{opx}} N_{\mathrm{A}}}{\mathrm{R}T^{\mathrm{pyx}}}\left[\frac{r_0^{\mathrm{opx}}}{2}\left(r_0^{\mathrm{opx}} - r_i\right)^2 - \frac{1}{3}\left(r_0^{\mathrm{opx}} - r_i\right)^3\right], \quad \text{(B1a)}$$

$$A_i^{\mathrm{cpx,amp}} = -7.14 + \frac{7.19\times10^4}{\mathrm{R}T^{\mathrm{pyx}}} + 4.37X_{\mathrm{Al}}^{\mathrm{T,cpx}} + 1.98X_{\mathrm{Mg}}^{\mathrm{M2,cpx}} + 4.21 - 1.52X_{\mathrm{Ti}}^{\mathrm{amp}} +$$

$$0.35X_{\mathrm{Mg}}^{\mathrm{amp}} + 1.83X_{\mathrm{Na}}^{\mathrm{amp}} + 2.95X_{\mathrm{K}}^{\mathrm{amp}} - \frac{4\pi E^{\mathrm{cpx}} N_{\mathrm{A}}}{\mathrm{R}T^{\mathrm{pyx}}}\left[\frac{r_0^{\mathrm{cpx}}}{2}\left(r_0^{\mathrm{cpx}} - r_i\right)^2 - \frac{1}{3}\left(r_0^{\mathrm{cpx}} - r_i\right)^3\right], \quad \text{(B1b)}$$

$$B_i^{\mathrm{amp}} = -\frac{7.27\times10^4}{\mathrm{R}} + \frac{4\pi E^{\mathrm{amp}} N_{\mathrm{A}}}{\mathrm{R}}\left[\frac{r_0^{\mathrm{amp}}}{2}\left(r_0^{\mathrm{amp}} - r_i\right)^2 - \frac{1}{3}\left(r_0^{\mathrm{amp}} - r_i\right)^3\right]. \quad \text{(B2)}$$

The lattice strain parameters r_0^{cpx}, E^{cpx}, r_0^{opx}, E^{opx}, r_0^{amp}, and E^{amp} are given in Appendix A.

References cited

Adam, J., and Green, T. (2003) The influence of pressure, mineral composition and water on trace element partitioning between clinopyroxene, amphibole and basanitic melts. European Journal of Mineralogy, 15, 831–841.

Adam, J., and Green, T. (2006) Trace element partitioning between mica-and amphibole-bearing garnet lherzolite and hydrous basanitic melt: 1. Experimental results and the investigation of controls on partitioning behaviour. Contributions to Mineralogy and Petrology, 152, 1–17.

Anders, E., and Grevesse, N. (1989) Abundances of the elements: meteoritic and solar. Geochimica et Cosmochimica Acta, 53, 197–214.

Aradi, L.E., Bali, E., Patkó, L., Hidas, K., Kovács, I.J., Zanetti, A., Garrido, C.J., and Szabo, C. (2020) Geochemical evolution of the lithospheric mantle beneath the

538 Styrian Basin (Western Pannonian Basin). Lithos, 378–379, 105831.
539 Belousov, I., Batanova, V., Sobolev, A., Savelieva, G., Danyushevsky, L., and Draayers, E.
540 (2021) Pyroxenites from mantle section of Voykar Ophiolite – Melt/peridotite
541 reaction and crystallization in SSZ mantle. Lithos, 388–389, 106063.
542 Bénard, A., and Ionov, D.A. (2013) Melt– and fluid–rock interaction in supra-subduction
543 lithospheric mantle: Evidence from andesite-hosted veined peridotite xenoliths.
544 Journal of Petrology, 54, 2339–2378.
545 Bénard, A., Müntener, O., Pilet, S., Arculus, R. J., and Nebel, O. (2021) Silica-rich spinel
546 harzburgite residues formed by fractional hybridization-melting of the intra-oceanic
547 supra-subduction zone mantle: new evidence from TUBAF seamount peridotites.
548 Geochimica et Cosmochimica Acta, 293, 477–506.
549 Blundy, J., and Wood, B. (1994) Prediction of crystal-melt partition coefficients from
550 elastic moduli. Nature, 372, 452–454.
551 Brey, G.P., and Köhler, T. (1990) Geothermobarometry in four-phase lherzolites II. New
552 thermobarometers, and practical assessment of existing thermobarometers. Journal
553 of Petrology, 31, 1353–1378.
554 Brice, J.C. (1975) Some thermodynamic aspects of the growth of strained crystals. J.
555 Cryst. Growth 28, 249–253.
556 Cherniak, D.J., and Liang, Y. (2007) Rare earth element diffusion in natural enstatite.
557 Geochimica et Cosmochimica Acta, 71, 1324–1340.
558 Coltorti, M., Bonadiman, C., Faccini, B., Gregoire, M., O'Reilly, S.Y., and Powell, W.
559 (2007) Amphiboles from suprasubduction and intraplate lithospheric mantle. Lithos,
560 99, 68–84.

561 Dimanov, A., and Wiedenbeck, M. (2006) (Fe, Mg)–Mg interdiffusion in natural diopside:
562 effect of pO_2. European Journal of Mineralogy, 18, 274–705.
563 Frost, D. J., and McCammon, C.A. (2008) The redox state of Earth's mantle. Annual
564 Review of Earth and Planetary Sciences, 36, 389–420.
565 Fumagalli, P., Zanchetta, S., and Poli, S. (2009) Alkali in phlogopite and amphibole and
566 their effects on phase relations in metasomatized peridotites: A high-pressure study.
567 Contributions to Mineralogy and Petrology, 158, 723–737.
568 Gaetani, G.A. (2004) The influence of melt structure on trace element partitioning near
569 the peridotite solidus. Contributions to Mineralogy and Petrology, 147, 511–527.
570 Gaetani, G.A., Kent, A.J., Grove, T. L., Hutcheon, I.D., and Stolper, E.M. (2003)
571 Mineral/melt partitioning of trace elements during hydrous peridotite partial melting.
572 Contributions to Mineralogy and Petrology, 145, 391–405.
573 Green, D.H. (1973) Experimental melting studies on a model upper mantle composition
574 at high pressure under water-saturated and water-undersaturated conditions. Earth
575 and Planetary Science Letters, 19, 37–53.
576 Gregoire, M., Lorand, J.P., O'Reilly, S.Y., and Cottin, J.Y. (2000) Armalcolite-bearing,
577 Ti-rich metasomatic assemblages in harzburgitic xenoliths from the Kerguelen
578 Islands: implications for the oceanic mantle budget of high-field strength elements.
579 Geochimica et Cosmochimica Acta, 64, 673–694.
580 Hawthorne, F.C., Oberti, R., Harlow, G.E., Maresch, W.V., Martin, R.F., Schumacher, J.C.,
581 and Welch, M.D. (2012) Nomenclature of the amphibole supergroup. American
582 Mineralogist, 97, 2031–2048.
583 Hellebrand E., Snow J. E., Mostefaoui S. and Hoppe P. (2005) Trace element distribution

584 between orthopyroxene and clinopyroxene in peridotites from the Gakkel Ridge: A
585 SIMS and NanoSIMS study. Contributions to Mineralogy and Petrology, 150, 486–
586 504.
587 Ishimaru, S., Arai, S., Ishida, Y., Shirasaka, M., and Okrugin, V.M. (2007) Melting and
588 multi-stage metasomatism in themantle wedge beneath a frontal arc inferred from
589 highly depleted peridotite xenoliths from the Avacha volcano, Southern Kamchatka.
590 Journal of Petrology, 48, 395–433.
591 Klein, M., Stosch, H. G., Seck, H. A., and Shimizu, N. (2000) Experimental partitioning
592 of high field strength and rare earth elements between clinopyroxene and garnet in
593 andesitic to tonalitic systems. Geochimica et Cosmochimica Acta, 64, 99–115.
594 Klein, M., Stosch, H.G., and Seck, H.A. (1997) Partitioning of high field-strength and
595 rare-earth elements between amphibole and quartz-dioritic to tonalitic melts: An
596 experimental study. Chemical Geology, 138, 257–271.
597 Leake, B.E., Woolley, A.R., Arps, C.E.S., Birch, W.D., Gilbert, M.C., Grice, J.D.,
598 Hawthorne, F.C., Kato, A., Kisch, H.J., Krivovichev, V.G., and others. (1997)
599 Nomenclature of amphiboles: report of the subcommittee on amphiboles of the
600 International Mineralogical Association, Commission on New Minerals and Mineral
601 Names. Canadian Mineralogist, 35, 219–246.
602 Lee, C.T.A., Harbert, A., and Leeman, W.P. (2007) Extension of lattice strain theory to
603 mineral/mineral rare-earth element partitioning: an approach for assessing
604 disequilibrium and developing internally consistent partition coefficients between
605 olivine, orthopyroxene, clinopyroxene and basaltic melt. Geochimica et
606 Cosmochimica Acta, 71, 481–496.

607 Liang, Y. (2015) A simple model for closure temperature of a trace element in cooling
608 bi-mineralic systems. Geochimica et Cosmochimica Acta, 165, 35–43.
609 Liang, Y., Sun, C., and Yao, L. (2013) A REE-in-two-pyroxene thermometer for mafic
610 and ultramafic rocks. Geochimica et Cosmochimica Acta, 102, 246–260.
611 Liu, C.Z., Wu, F.Y., Wilde, S.A., Yu, L.J., and Li, J.L. (2010). Anorthitic plagioclase and
612 pargasitic amphibole in mantle peridotites from the Yungbwa ophiolite
613 (southwestern Tibetan Plateau) formed by hydrous melt metasomatism. Lithos,
614 114(3–4), 413–422.
615 Mandler, B.E., and Grove, T.L. (2016) Controls on the stability and composition of
616 amphibole in the Earth's mantle. Contributions of Mineralogy and Petrology, 171,
617 1–20.
618 Matusiak-Małek, M., Puziewicz, J., Ntaflos, T., Grégoire, M., Kukuła, A., and Wojtulek,
619 P.M. (2017) Origin and evolution of rare amphibole-bearing mantle peridotites from
620 Wilcza Góra (SW Poland), Central Europe. Lithos, 286–287, 302–323.
621 Molina, J.F., Moreno, J.A., Castro, A., Rodruiguez, C., and Fershtater, G.B. (2015) Calcic
622 amphibole thermobarometry in metamorphic and igneous rocks: new calibrations
623 based on plagioclase/amphibole Al-Si partitioning and amphibole-liquid Mg
624 partitioning. Lithos, 232, 286–305.
625 Müller, T., Dohmen, R., Becker, H. W., ter Heege, Jan H., and Chakragorty, S. (2013) Fe–
626 Mg interdiffusion rates in clinopyroxene: experimental data and implications for Fe–
627 Mg exchange geothermometers. Contributions of Mineralogy and Petrology, 166,
628 1563–1576.
629 Niida, K., and Green, D.H. (1999) Stability and chemical composition of pargasitic

amphibole in MORB pyrolite under upper mantle conditions. Contributions to Mineralogy and Petrology, 135, 18–40.

Nishio, I., Morishita, T., Itano, K., Guotana, J. M., Tamura, A., Szilas, K., Harigane, Y., Tani, K., and Pearson, D.G. (2022) Metasomatic modification of the Mesoarchaean Ulamertoq ultramafic body, southern West Greenland. Journal of Petrology, 63, 3.

Pintér, Z., Patkó, L., Djoukam, J.F.T., Kovács, I., Tchouankoue, J.P., Falus, G., Konc, Z., Tommasi, A., Barou, F., Mihály, J., Németh, C., and Jeffries, T. (2015) Characterization of the sub-continental lithospheric mantle beneath the Cameron volcanic line inferred from alkaline basalt hosted peridotite xenoliths from Barombi Mbo and Nyos Lakes. Journal of African Earth Sciences, 111, 170–193.

Putirka, K.D. (2008) Thermometers and barometers for volcanic systems. Reviews in Mineralogy and Geochemistry, 69, 61–120.

Putirka. (2016) Amphibole thermometers and barometers for igneous systems and some implications for eruption mechanisms of felsic magmas at arc volcanoes. American Mineralogist, 101, 841–858.

Puziewicz, J., Aulbach, S., Kaczmarek, M.A., Ntaflos, T., Gerdes, A., Mazurek, H., Kukuła, A., and Ziobro-Mikrut, M. (2023) The origin and evolution of DMM-like lithospheric mantle beneath continents: Mantle xenoliths from the Oku Volcanic Group in the Cameroon Volcanic Line, West Africa. *Journal of Petrology*, *64*, egad049.

Rapp, R.P., Shimizu, N., Norman, M.D., and Applegate, G.S. (1999) Reaction between slab-derived melts and peridotite in the mantle wedge: Experimental constraints at 3.8 GPa. Chemical Geology, 160, 335–356.

653 Ridolfi, F., and Renzulli, A. (2012) Calcic amphiboles in calc-alkaline and alkaline
654 magmas: thermobarometric and chemometric empirical equations valid up to
655 1,130 °C and 2.2 GPa. Contributions to Mineralogy and Petrology, 163, 877–895.
656 Sen, C., and Dunn, T. (1994) Experimental modal metasomatism of a spinel lherzolite
657 and the production of amphibole-bearing peridotite. Contributions to Mineralogy
658 and Petrology, 119, 422–432.
659 Shannon, R.D. (1976) Revised effective ionic radii and systematic studies of interatomic
660 distances in halides and chalcogenides. Acta crystallographica section A: crystal
661 physics, diffraction, theoretical and general crystallography, 32(5), 751–767.
662 Shimizu, K., Sun, C., Liang, Y., Jackson, C.R.M., and Saal, A.E. (2017) Parameterized
663 lattice strain models for REE partitioning between amphibole and silicate melt.
664 American Mineralogist, 102, 2254–2267.
665 Stosch, H.G. (1982) Rare earth element partitioning between minerals from anhydrous
666 spinel peridotite xenoliths. Geochimica et Cosmochimica Acta, 46, 793–811.
667 Sun, C., and Liang, Y. (2012) Distribution of REE between clinopyroxene and basaltic
668 melt along a mantle adiabat: Effects of major element composition, water, and
669 temperature. Contributions to Mineralogy and Petrology, 163, 807–823.
670 Sun, C., and Liang, Y. (2013) Distribution of REE and HFSE between low-Ca pyroxene
671 and lunar picritic melts around multiple saturation points. Geochimica et
672 Cosmochimica Acta, 119, 340–358.
673 Sun, C., and Liang, Y. (2014) An assessment of subsolidus re-equilibration on REE
674 distribution among mantle minerals olivine, orthopyroxene, clinopyroxene, and
675 garnet in peridotites. Chemical Geology, 372, 80–91.

676 Van Orman, J.A., Grove, T.L., and Shimizu N. (2001) Rare earth element diffusion in
677 diopside: influence of temperature, pressure, and ionic radius, and an elastic model
678 for diffusion in silicates. Contributions to Mineralogy and Petrology, 141, 687–703.
679 Van Orman, J.A., Grove, T.L., and Shimizu N. (2002) Diffusion fractionation of trace
680 elements during production and transport of melt in Earth's upper mantle. Earth and
681 Planetary Science Letters, 198, 93–112.
682 Wallace, M.E., and Green, D.H. (1991) The effect of bulk rock composition on the
683 stability of amphibole in the upper mantle. Mineralogy and Petrology, 44, 1–19.
684 Wang, C., Liang, Y., and Xu, W. (2021) Formation of amphibole-bearing peridotite and
685 amphibole-bearing pyroxenite through hydrous melt-peridotite reaction and in situ
686 crystallization: an experimental study. Journal of Geophysical Research, Solid Earth,
687 126, e2020JB019382. https://doi.org/10.1029/2020JB019382.
688 Wells, P.R. (1977) Pyroxene thermometry in simple and complex systems. Contributions
689 to Mineralogy and Petrology, 62, 129–139.
690 Witt-Eickschen, G., Palme, H., O'Neill, H.S.C., and Allen, C. (2009) The geochemistry
691 of the volatile trace elements As, Cd, Ga, In and Sn in the Earth's mantle: New
692 evidence from in situ analyses of mantle xenoliths. Geochimica et Cosmochimica
693 Acta, 73, 1755–1778.
694 Witt-Eickschen, G., and O'Neill, H.S.C. (2005) The effect of temperature on the
695 equilibrium distribution of trace elements between clinopyroxene, orthopyroxene,
696 olivine, and spinel in upper mantle peridotite. Chemical Geology, 221, 65–101.
697 Witt-Eickschen, G., and Seck, H.A. (1991) Solubility of Ca and Al in orthopyroxene from
698 spinel peridotite: An improved version of an empirical geothermometer.

699 Contributions to Mineralogy and Petrology, 106, 431–439.

700 Wood, B.J., and Banno, S. (1973) Garnet–orthopyroxene and orthopyroxene–
701 clinopyroxene relationships in simple and complex systems. Contributions to
702 Mineralogy and Petrology, 42, 109–124.

703 Wood, B.J., and Blundy, J.D. (1997) A predictive model for rare earth element
704 partitioning between clinopyroxene and anhydrous silicate melt. Contributions to
705 Mineralogy and Petrology, 129, 166–181.

706 Wood, B.J., and Blundy, J. (2003) Trace element partitioning under crustal and uppermost
707 mantle conditions: The influences of ionic radius, cation charge, pressure, and
708 temperature. Treatise on Geochemistry, 2, 395–424.

709 Wood, B.J., and Blundy, J.D. (2002) The effect of H_2O on crystal-melt partitioning of
710 trace elements. Geochimica et Cosmochimica Acta, 66, 3647–3656.

711 Xu, W., Yang, D., Gao, S., Pei, F., and Yu, Y. (2010) Geochemistry of peridotite xenoliths
712 in early Cretaceous high-Mg# diorites from the central orogenic block of the North
713 China Craton: The nature of Mesozoic lithospheric mantle and constraints on
714 lithospheric thinning. Chemical Geology, 270, 257–273.

715 Yao, L., Sun, C. and Liang, Y. (2012) A parameterized model for REE partitioning
716 between low-Ca pyroxene and basaltic melts with applications to adiabatic mantle
717 melting and pyroxenite-derived melt and peridotite interaction. Contributions to
718 Mineralogy and Petrology, 164, 261–280.

719 Zhang, Z.Y., Liu, C.Z., Liang, Y., Zhang, C., Liu, T., Zhang, W.Q., and Ji, W.B. (2022).
720 Decoupled trace element and isotope compositions recorded in orthopyroxene and
721 clinopyroxene in composite pyroxenite veins from the Xiugugabu Ophiolite (SW

722 Tibet). Journal of Petrology, 63, 1–28.

723 Zhou, Q. (2014) Petrogenesis of wehrlite and pyroxenite xenoliths in early Cretaceous
724 igneous Rocks from western Shandong, China. (Ph.D. Thesis), Jilin University,
725 Changchun (in Chinese with English abstract).

726

Figure captions

Figure 1. Compositions of amphiboles (oxides in wt%, on volatile-free basis) from amphibole-bearing mantle rocks. Red and blue plus signs are intraplate (I)-amphiboles and supra-subduction (S)-amphiboles, respectively, classified after Coltroti et al. (2007). Green dots are amphiboles from the amphibole–melt REE partitioning experiments used to calibrate the model of Shimizu et al. (2017). Closed symbols are amphiboles in mantle samples that have compositions within the range of those used for calibration. The calculation of chemical formulae and the compositional boundaries in (e) follow those of Leake et al. (1997). Tr, tremolite; Ath, anthophyllite; Fac, ferro-actinolite; Gru, grunerite.

Figure 2. Correlations of temperature derived from the REE-in-two-pyroxene thermometer of Liang et al. (2013, T_{REE}) with those from the major element-based two-pyroxene thermometers of Brey and Köhler (1990, T_{BKN}), Wells (1977, T_{W77}), Putirka (2008, his Eq. (37), T_{P37}), and average of the three (T_{avg}) for the amphibole-bearing mantle rocks. Symbols are the same as in Fig. 1. Error bars are 1σ uncertainties in T_{REE}. The solid gray lines in denote the 1:1 correlation, and the dashed gray lines denote the ±100°C deviations. Gray fields show the ranges of temperatures of well-equilibrated peridotite xenoliths from Liang et al. (2013).

Figure 3. Comparisons of amphibole Mg# with orthopyroxene and clinopyroxene Mg#s for the amphibole-bearing mantle samples. Symbols with cross denote samples that display obvious textual and compositional disequilibrium. See text for details.

Figure 4. (a) Inversion diagram for the REE-in-two-pyroxene temperature (T_{REE}) of an amphibole-bearing lherzolite (sample WLK30 from Wilcza Góra, SW Poland,

Matusiak-Malek et al., 2017). **(b–d).** Comparisons of the measured orthopyroxene–clinopyroxene and pyroxene–amphibole REE partition coefficients (solid red patterns) with those calculated using the mineral–mineral REE partitioning model of Eq. (2) at the inverted T_{REE} (solid blue curves). Partition coefficients calculated at 750°C, 925°C, and 1100°C are also shown for comparison (dashed blue isotherms). The partition coefficients are plotted against 8-fold ionic radii of REEs from Shannon (1976).

Figure 5. (a and **b).** Inversion diagrams for the apparent amphibole temperatures ($T^{amp,opx–amp}$ and $T^{amp,cpx–amp}$) of sample WLK30 (the lherzolite sample shown in Fig. 4) using our semi-empirical models. **(c** and **d).** Comparisons of the measured pyroxene–amphibole REE partition coefficients (solid red patterns) with those calculated using the REE partitioning models of Eq. (5) with amphibole temperature at the inverted $T^{amp,opx–amp}$ or $T^{amp,cpx–amp}$ (solid green curves). Partition coefficients calculated assuming the amphibole temperature at T_{REE}, T_{REE} − 100°C, and T_{REE} − 200°C are plotted for comparison (dot-dashed green isotherms). The partition coefficients are plotted against 8-fold ionic radii of REEs from Shannon (1976).

Figure 6. Comparisons of the T^{amp} calculated using Eq. (8) with **(a)** the inverted T^{amp} (average value of $T^{amp,opx–amp}$ and $T^{amp,cpx–amp}$), **(b)** T_{REE}, and **(c–f)** major-element derived temperatures for the amphibole-bearing mantle rocks. Symbols are the same as in Fig. 1, and the element-based two-pyroxene thermometers are identical to those in Fig. 2. The solid gray lines in denote the 1:1 correlation, and the dashed gray lines denote the ±50°C deviations.

Figure 7. Comparison between the measured pyroxene-amphibole REE partition

coefficients with those predicted using the partitioning models of Eq. (5) and T^{amp} calculated using Eq. (8). The solid gray lines in **(a** and **c)** denote the 1:1 correlation, and the dashed gray lines denote the 1:2 and 2:1 correlations. Data in **(a** and **c)** are color-coded with 8-fold ionic radii of REEs from Shannon (1976).

Figure 8. Patterns of pyroxene–amphibole REE partition coefficients calculated from the partitioning model of Eq. (5) with T^{amp} assumed to be 50–300°C lower than the T^{pyx} (assigned as T_{REE}) for the lherzolites WLK30 from Wilcza Góra (Matusiak-Małek et al., 2017) and AUB1407 from the Western Pannonian Basin, Hungary (Aradi et al., 2020). See text for discussions.

Figure 9. Chondrite-normalized REE patterns of amphiboles calculated using the semi-empirical pyroxene-amphibole REE partitioning models and REE contents in the coexisting pyroxenes for amphibole-bearing peridotite xenoliths **(a)** WG5 and WG6 from Wilcza Góra (Matusiak-Małek et al., 2017), **(b)** KPFS0402 and PST1403 from Western Pannonian Basin (Aradi et al., 2020), and **(c)** H71 and **(d)** H69 from Cameroon volcanic line (Puziewicz et al., 2023). Gray patterns in **(d)** were calculated using T^{amp} inverted from Eq. (7), which testifies the effect of heating. Also plotted for comparison are measured REE patterns of amphiboles in the Wilcza Góra xenoliths genetically related to WG5 and WG6 (Matusiak-Małek et al., 2017), Western Pannonian Basin xenoliths genetically related to KPFS0402 and PST1403 (Aradi et al., 2020), and Cameroon xenoliths H71 and H69 (Puziewicz et al., 2023). The chondrite REE abundances are from Anders and Grevesse (1989).

This is the peer-reviewed, final accepted version for American Mineralogist, published by the Mineralogical Society of America.
The published version is subject to change. Cite as Authors (Year) Title. American Mineralogist, in press.
DOI: https://doi.org/10.2138/am-2022-8831. http://www.minsocam.org/

Figure 1

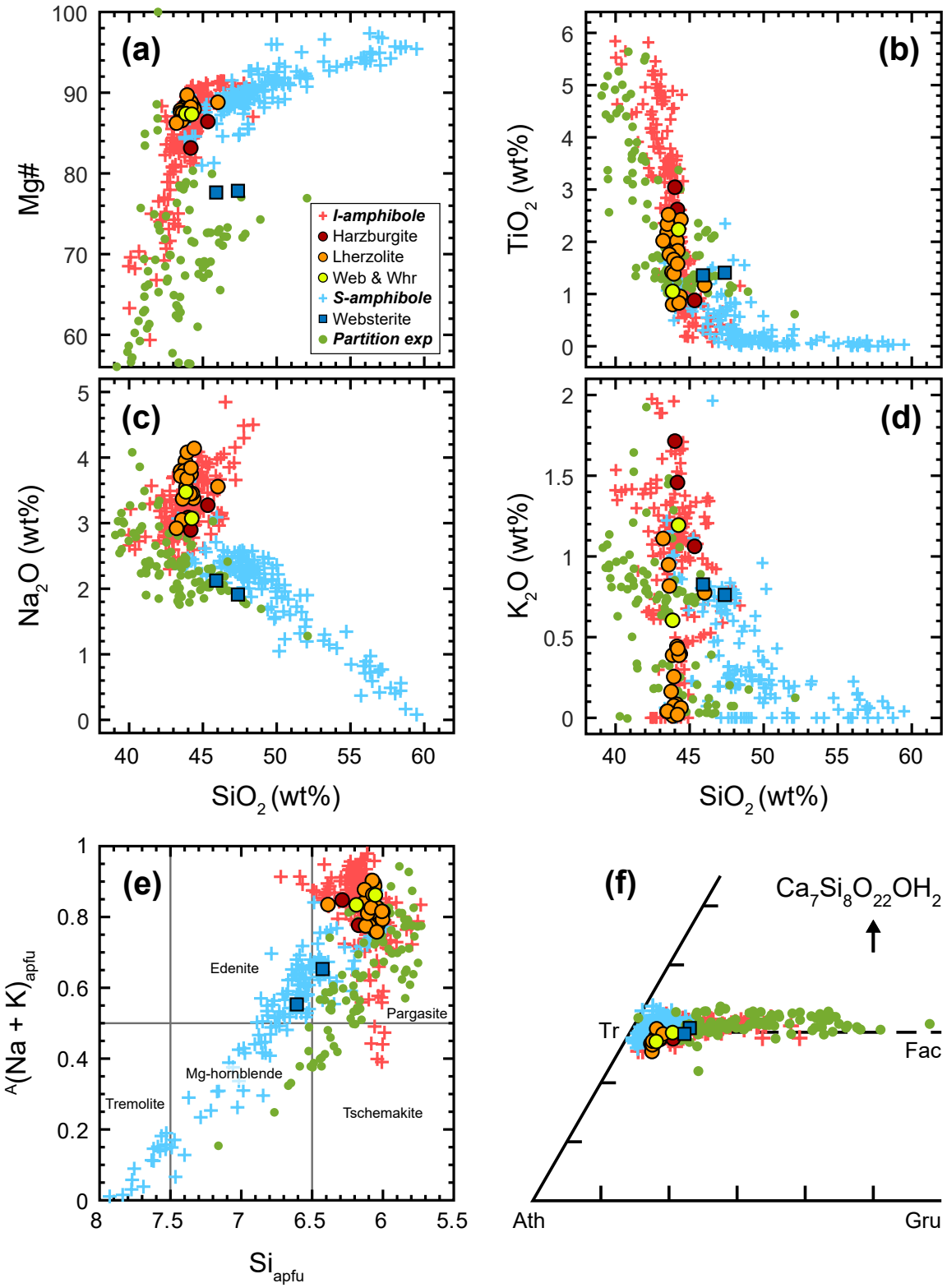

This is the peer-reviewed, final accepted version for American Mineralogist, published by the Mineralogical Society of America.
The published version is subject to change. Cite as Authors (Year) Title. American Mineralogist, in press.
DOI: https://doi.org/10.2138/am-2022-8831. http://www.minsocam.org/

Figure 2

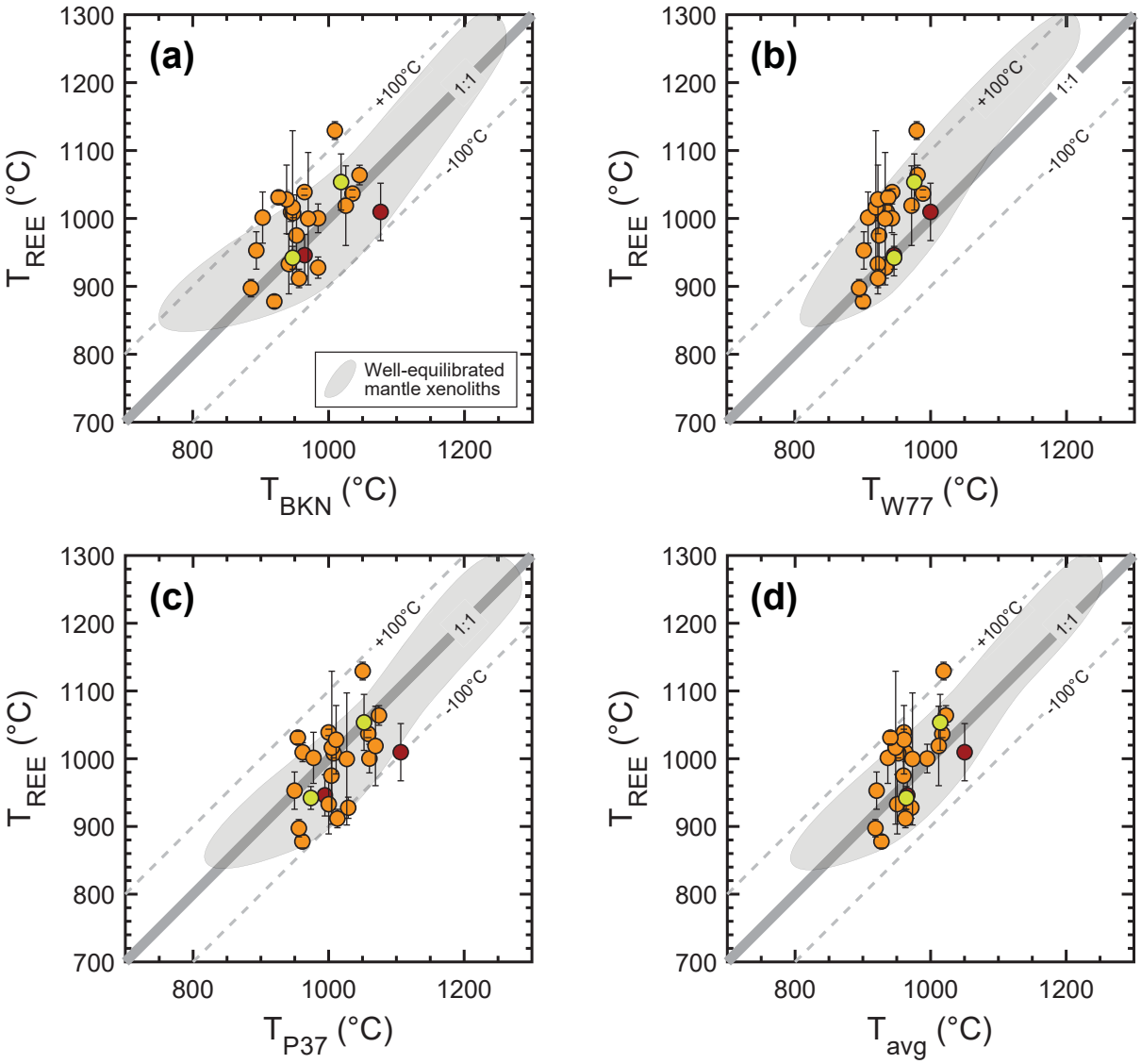

This is the peer-reviewed, final accepted version for American Mineralogist, published by the Mineralogical Society of America.
The published version is subject to change. Cite as Authors (Year) Title. American Mineralogist, in press.
DOI: https://doi.org/10.2138/am-2022-8831. http://www.minsocam.org/

Figure 3

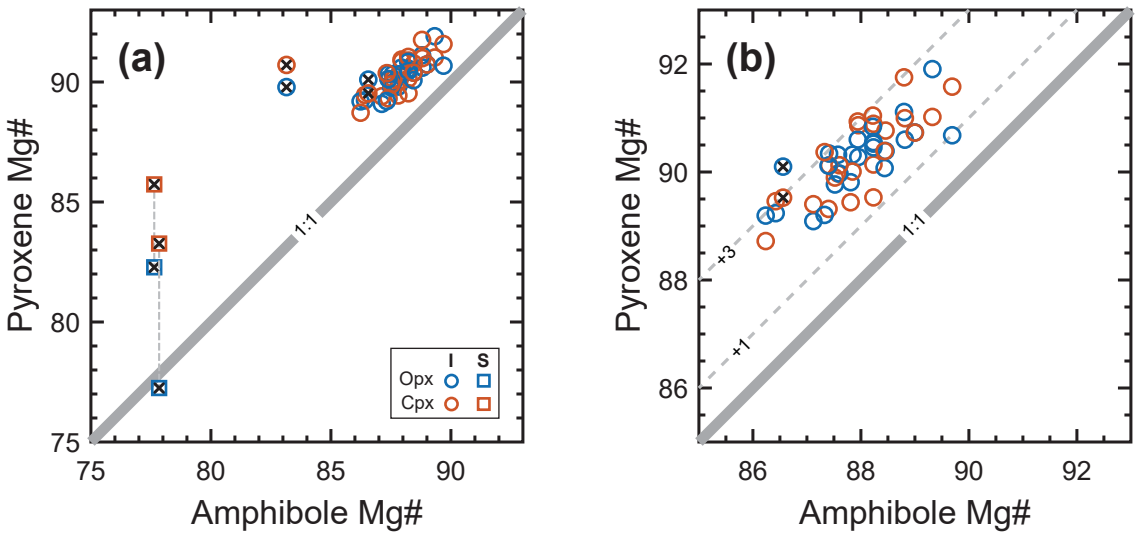

This is the peer-reviewed, final accepted version for American Mineralogist, published by the Mineralogical Society of America.
The published version is subject to change. Cite as Authors (Year) Title. American Mineralogist, in press.
DOI: https://doi.org/10.2138/am-2022-8831. http://www.minsocam.org/

Figure 4

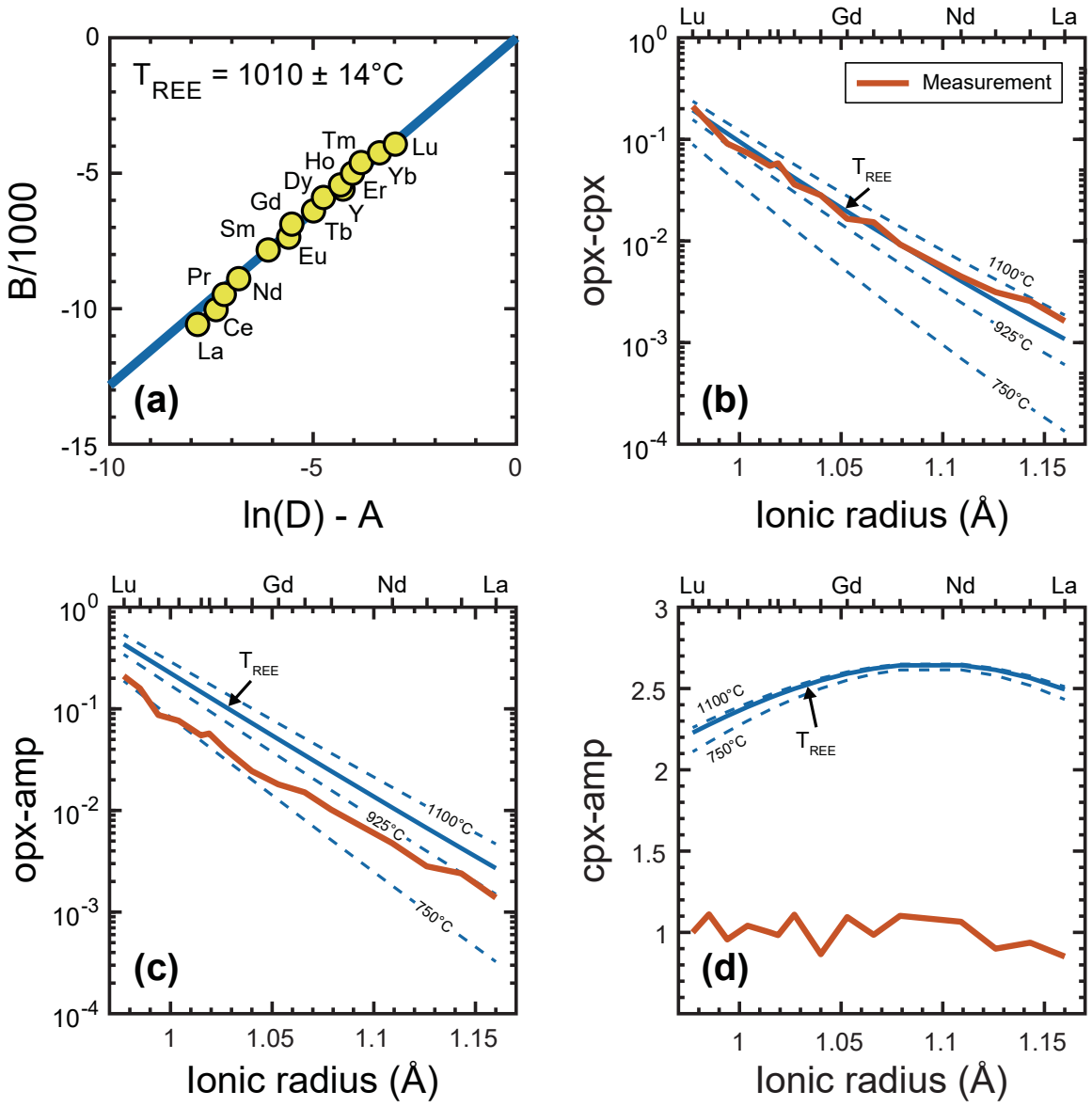

This is the peer-reviewed, final accepted version for American Mineralogist, published by the Mineralogical Society of America.
The published version is subject to change. Cite as Authors (Year) Title. American Mineralogist, in press.
DOI: https://doi.org/10.2138/am-2022-8831. http://www.minsocam.org/

Figure 5

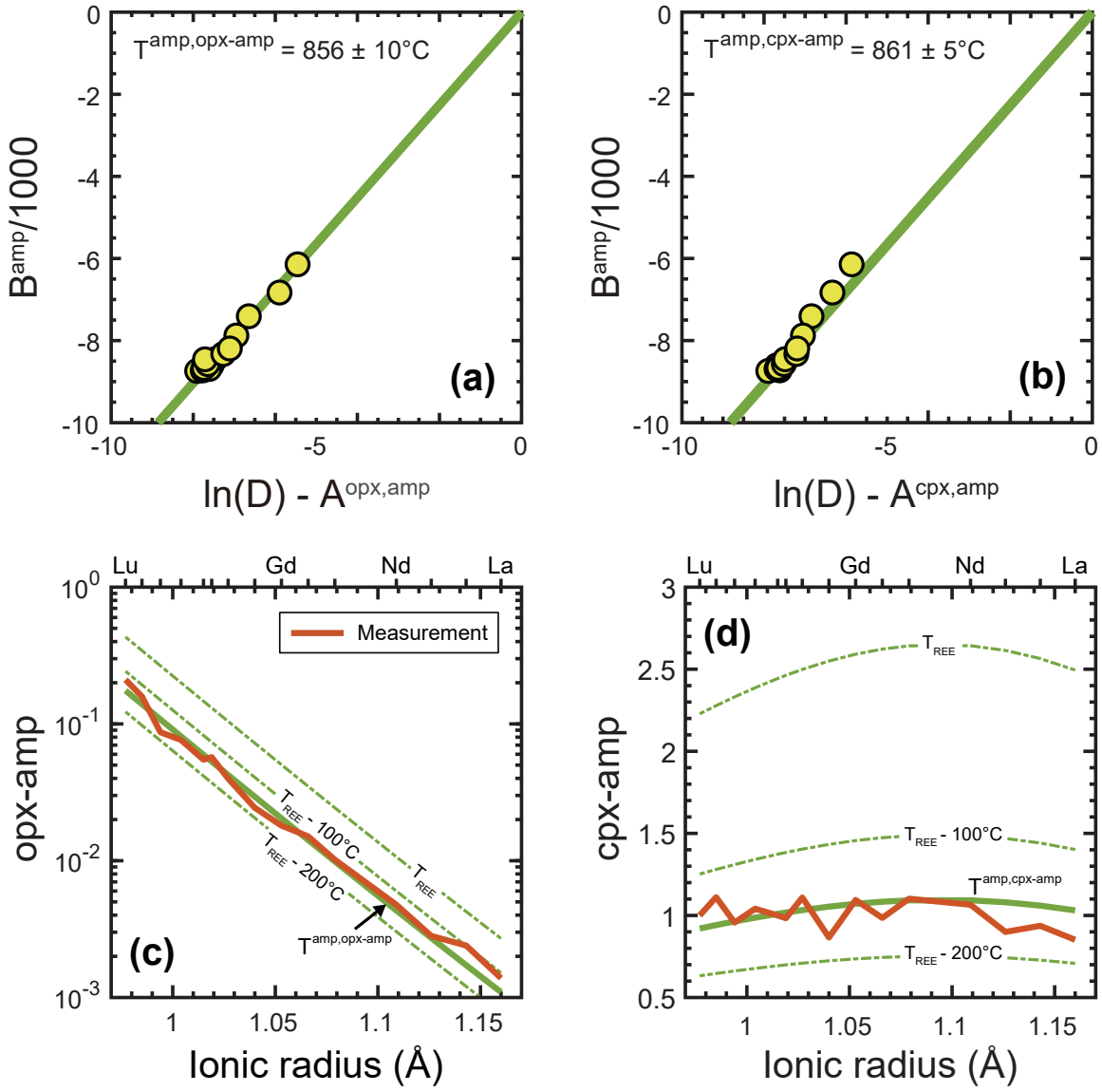

This is the peer-reviewed, final accepted version for American Mineralogist, published by the Mineralogical Society of America.
The published version is subject to change. Cite as Authors (Year) Title. American Mineralogist, in press.
DOI: https://doi.org/10.2138/am-2022-8831. http://www.minsocam.org/

Figure 6

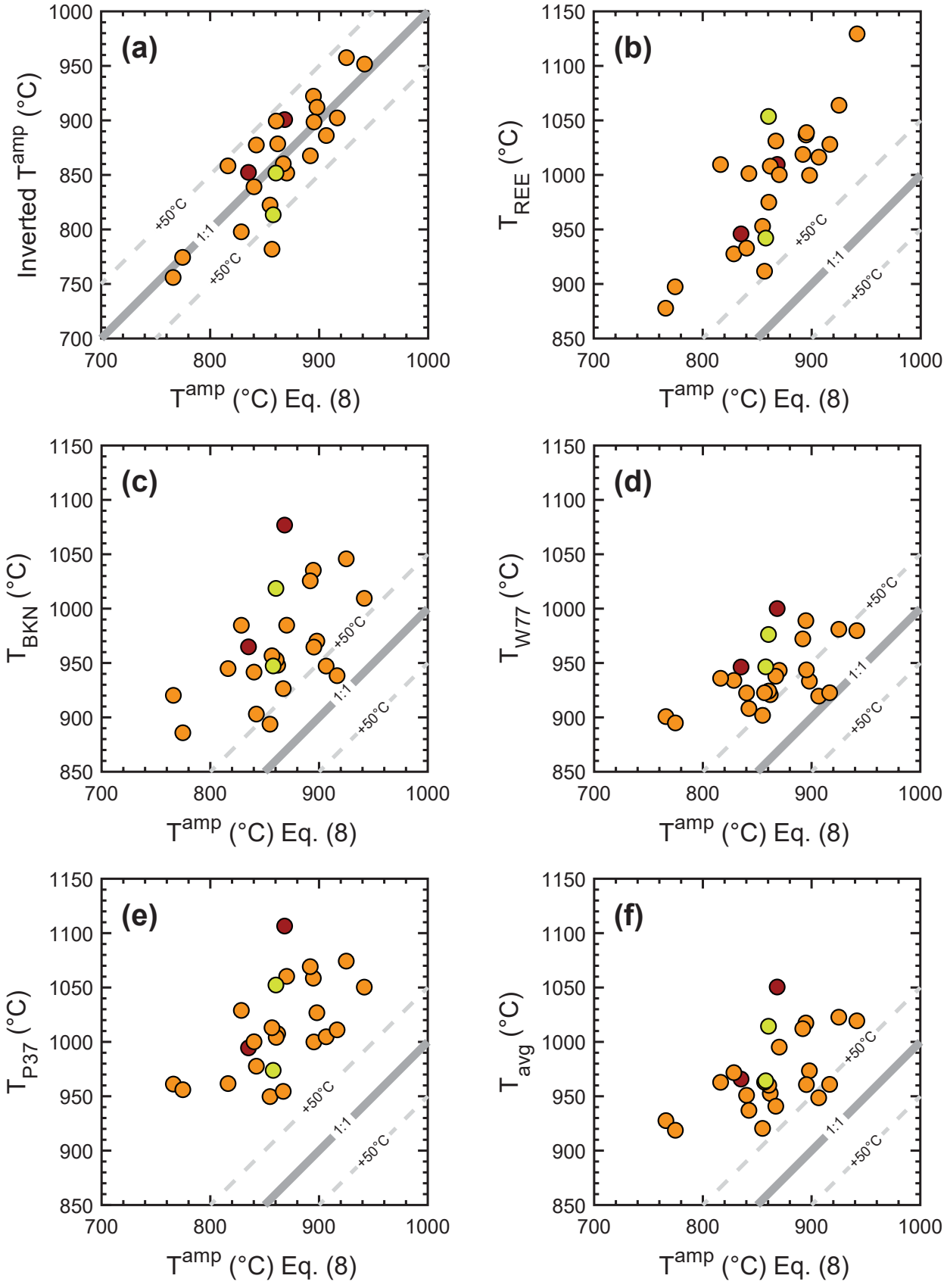

This is the peer-reviewed, final accepted version for American Mineralogist, published by the Mineralogical Society of America.
The published version is subject to change. Cite as Authors (Year) Title. American Mineralogist, in press.
DOI: https://doi.org/10.2138/am-2022-8831. http://www.minsocam.org/

Figure 7

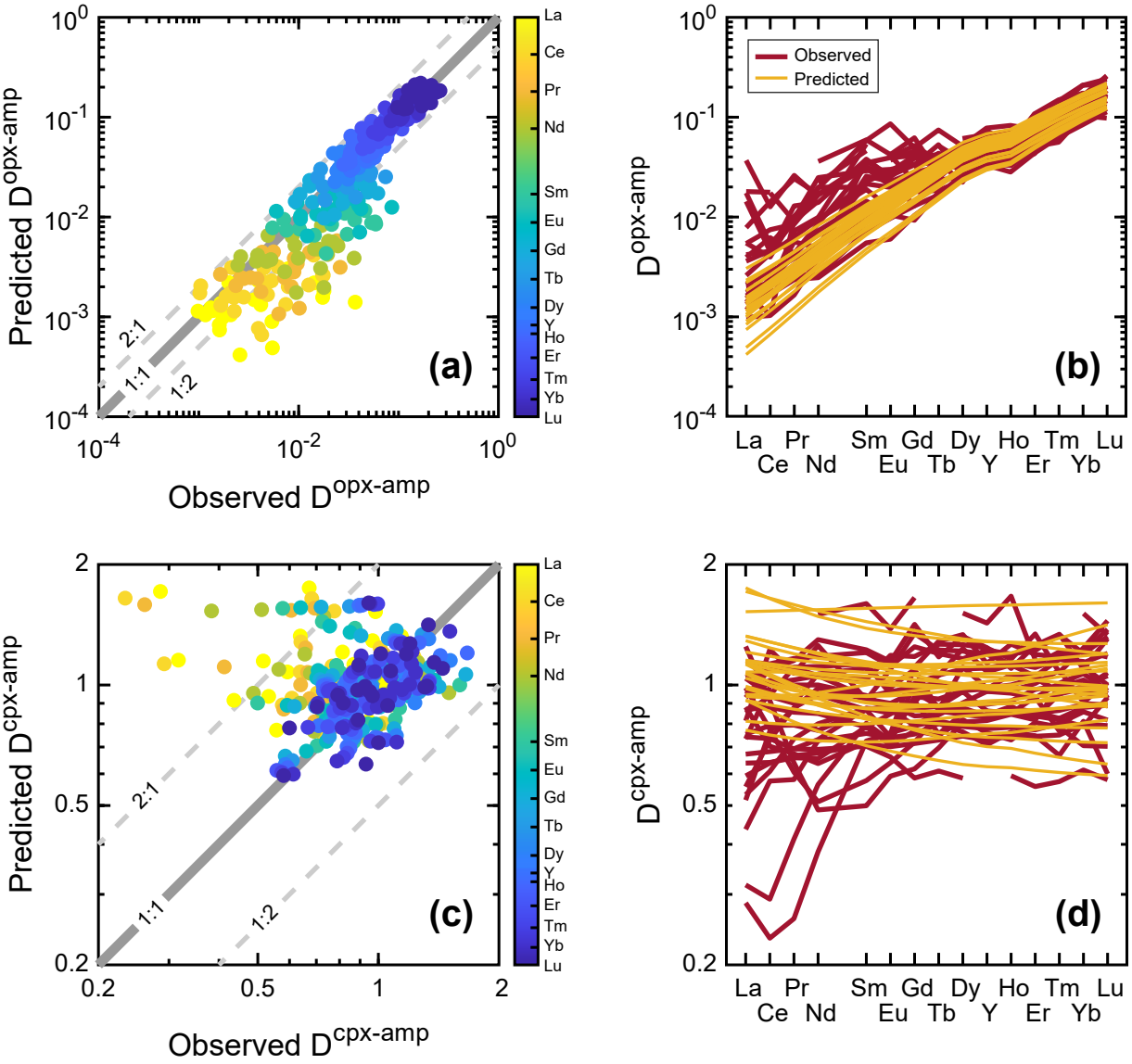

This is the peer-reviewed, final accepted version for American Mineralogist, published by the Mineralogical Society of America.
The published version is subject to change. Cite as Authors (Year) Title. American Mineralogist, in press.
DOI: https://doi.org/10.2138/am-2022-8831. http://www.minsocam.org/

Figure 8

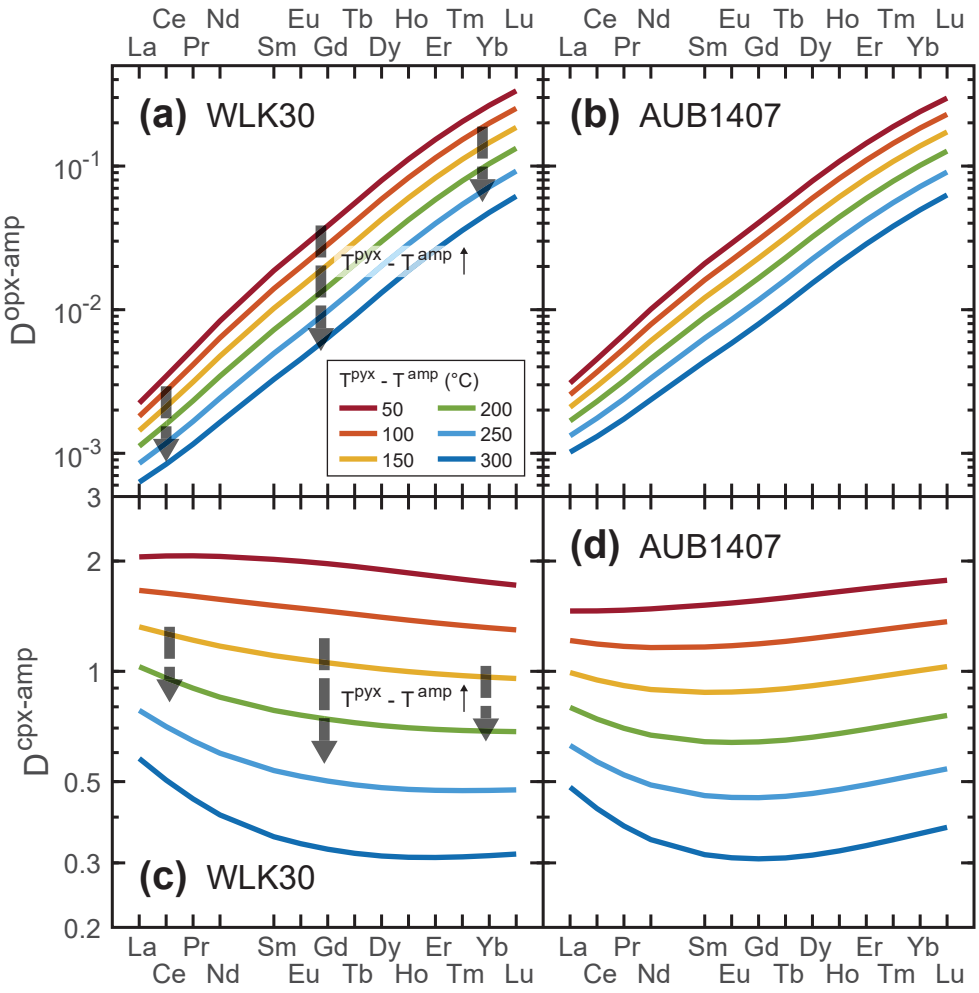

This is the peer-reviewed, final accepted version for American Mineralogist, published by the Mineralogical Society of America.
The published version is subject to change. Cite as Authors (Year) Title. American Mineralogist, in press.
DOI: https://doi.org/10.2138/am-2022-8831. http://www.minsocam.org/

Figure 9